RSGaussian: 3D Gaussian Splatting with LiDAR for Aerial Remote Sensing Novel View Synthesis

Yiling Yao^{a,b,c}, Wenjuan Zhang^{a,*}, Bing Zhang^{a,c}, Bocheng Li^{a,c}, Yaning Wang^{a,c}, Bowen Wang^a

Abstract—This study presents RSGaussian, an innovative novel view synthesis (NVS) method for aerial remote sensing scenes that incorporate LiDAR point cloud as constraints into the 3D Gaussian Splatting method, which ensures that Gaussians grow and split along geometric benchmarks, addressing the overgrowth and floaters issues occurs. Additionally, the approach introduces coordinate transformations with distortion parameters for camera models to achieve pixel-level alignment between LiDAR point clouds and 2D images, facilitating heterogeneous data fusion and achieving the high-precision geoalignment required in aerial remote sensing. Depth and plane consistency losses are incorporated into the loss function to guide Gaussians towards real depth and plane representations, significantly improving depth estimation accuracy. Experimental results indicate that our approach has achieved novel view synthesis that balances photo-realistic visual quality and highprecision geometric estimation under aerial remote sensing datasets. Finally, we have also established and open-sourced a dense LiDAR point cloud dataset along with its corresponding aerial multi-view images, AIR-LONGYAN.

Keywords— Novel view synthesis, 3D reconstruction, 3D Gaussian Splatting, LiDAR point cloud, Aerial remote sensing.

1. Introduction

Novel view synthesis (NVS) is a challenging task which aims to generate new images from unseen perspectives by learning scene information from captured multi-view images. It holds significance for applications such as object recognition, real-scene 3D and low-altitude economy. In aerial remote sensing, this technology primarily relies on Oblique photogrammetry technology [1], [2], which employs multi-view images captured under a designed flight path as input [3]. Through algorithms such as Structure from Motion (SfM) [4], Multi-View Stereo (MVS) [5], and the principle of bundle adjustment [6], it can efficiently collect data and reconstruct 3D models of the target area. By projecting 3D information from a specific viewpoint, a novel view image synthesis is achieved [7].

However, this technique employs texture mapping [8] to depict appearance, failing to consider 3D radiometric attributes, resulting in a significant difference between the spectral radiance values of the synthesized image and ground truth [9]. For example, in **Fig. 1**, ground truth (a) appears generally

yellow, whereas the newly generated view (b) is bluish. Meanwhile, it employs triangular meshes [10] to represent the scene structure, which can only recover the approximate geometric structure and lacks details, as shown in the red circle in **Fig. 1**, where the cylinder and its shadow in ground truth are incorrectly represented as a flat trapezoid.

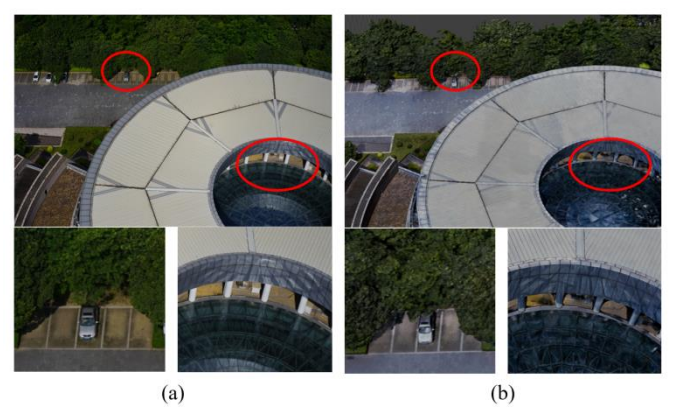


Fig. 1. Disadvantages of traditional NVS methods. (a)Ground truth, (b) Novel view image synthesized by oblique photogrammetry.

In recent years, many innovative novel view synthesis methods have emerged in the fields of computer vision and computer graphics, with the most impressive results coming from Neural Radiance Fields (NeRF) [11] and 3D Gaussian Splatting (3DGS) [12]. NeRF combines neural networks and volume rendering techniques to train an implicit neural radiance field model capable of synthesizing novel view images from arbitrary viewpoints. However, the computational overhead of the volume rendering process is substantial, often resulting in training and rendering times that can span dozens of hours. Despite numerous optimization efforts [13], [14], [15], [16], NeRF still faces the challenge of slow rendering speed, and its implicit expression lacks geometric entities and cannot express geometric structure accuracy, making it difficult to promote the quantitative application of large scenes.

3D Gaussian Splatting (3DGS) [12] has emerged as a significant advancement in the field of computer vision and computer graphics, achieving real-time photo-realistic novel view synthesis. It uses a novel representation called Gaussians

^aAerospace Information Research Institute, Chinese Academy of Sciences, Beijing 100094, China,

^bInternational Research Center of Big Data for Sustainable Development Goals, Beijing 100094, China

^cCollege of Resources and Environment, University of Chinese Academy of Sciences, Beijing 100049, China

to represent scenes, which expresses geometry with ellipsoids described by Gaussian distributions and expresses appearance with spherical harmonics to fit the anisotropy of radiation, The main process can be divided into three steps:

- Initialization: 3DGS first estimates a sparse point cloud from multi-view images using the SFM algorithm as initialization, providing an initial geometric framework for the model. Then, it begins to grow Gaussians on the initialized point cloud.
- 2) Gaussians Densification: 3DGS adaptively controls the densification growth of Gaussians. For Gaussians whose gradients in view space exceed a threshold, small Gaussians are cloned in under-reconstructed regions, or large Gaussians are split in over-reconstructed regions.
- 3) Gaussians Regularization: In the parameter regularization, the loss function is minimized via backpropagation to optimize the parameters of the Gaussians' covariance matrices (which define the size and shape of the Gaussians) and spherical harmonics (used to describe the appearance characteristics of the Gaussians).

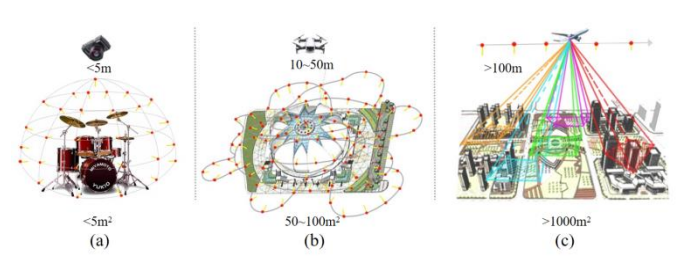


Fig. 2. Comparison of different scenes. (a) Close-range, small-scale and object-centric scene, (b) large-scale scene, (c) aerial remote sensing scene.

In the early research, 3DGS was mainly applied to closerange, small-scale and object-centric scenes(shown in Fig. 2 (a)), achieving realistic novel view synthesis [17], [18], [19], [20]. However, when the scene extends to a large-scale, such as streets- or city-scale, due to the vastness of the scenery(shown in **Fig. 2** (b)), leading to two primary issues: Firstly, the distance between the camera and the scene increased, and simultaneously, the number of effective viewpoints was significantly reduced due to the pose limitations of the aircraft. These two factors together led to errors in depth estimation during the initialization and densification of Gaussians, resulting in noticeable floaters and artifacts in the synthesized images [21] as indicated by the red circle in Fig. 3. Secondly, the ground resolution decreased, with limited visual prior knowledge, and without explicit constraints on true geometric structures, the Gaussians tended to over-stretching in the area which should have geometric consistency during the densification or regularization process [22], as indicated by the blue circle in Fig. 3, causing the constructed Gaussians to deviate from the actual structure, thus leading to low reconstruction accuracy in these areas.

To address these issues. VastGaussian[17] [21] introduces

a progressive partitioning strategy to segment a large scene into multiple cells, ensuring that training images are distributed appropriately based on an airspace-aware visibility effectively mitigating floaters occurrences. criterion, Gaussianpro [22] employs patch-matching techniques to generate normal maps and formulates a progressive Gaussian propagation strategy that guides the densification of Gaussians, thereby resolving the suboptimal reconstruction performance of 3DGS in outdoor scenes. Pixel-gs [23] introduces a dynamic scaling of the gradient field based on the distance from the scene to the camera, aiming to suppress the growth of blurring and needle-like artifacts that arise in regions with insufficient initial points. Gs-slam [24] employs synchronously acquired RGBD cameras as depth priors to control the densification of Gaussians. Most of the above improvements mainly enhance the applicability of the 3DGS method in large-scale scenes by designing algorithms that are closer to the geometric characteristics of large scenes, including using purely visual algorithms to generate depth as prior or acquiring depth priors with the help of RGBD cameras.

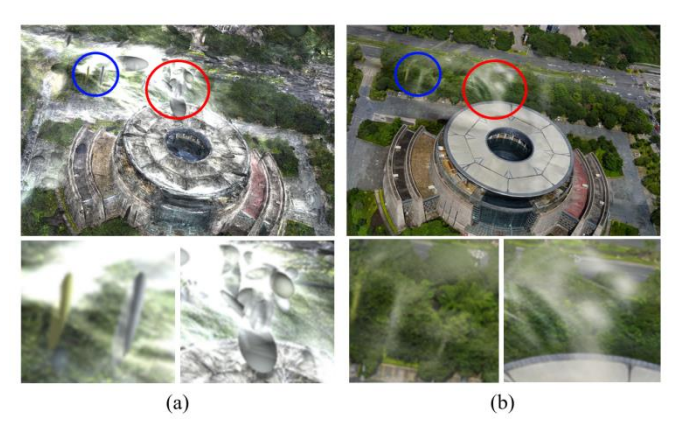


Fig. 3. Issues occur in large-scale scenes with 3DGS. (a) Gaussians distribution, (b) Rendered image.

However, aerial remote sensing applications differ from ordinary large scenes(shown in **Fig. 2** (c)). The observation areas are often much broader, and the distance between the sensor and the ground is much greater than the effective working range of RGBD cameras [25]. Moreover, the acquisition of aerial remote sensing data mainly relies on airborne or satellite cameras, which typically provide limited observation angles. For example, the Microsoft UltraCam Osprey [26] and Trimble UX5 HP [27] carried by drones can only provide five observation angles, with flight heights reaching hundreds of meters; the Airborne Multi-angular TIR/VNIR Imaging System (AMTIS) provides nine observation angles, with flight heights reaching thousands of meters [28]; and the POLDER satellite, which uses a wide swath two-dimensional CCD, can obtain up to 16 angles of observation data in a single orbit, with an orbital height of 705 kilometers [29]. Finally, aerial remote sensing applications not only require realistic visualization results but also emphasize high-precise quantitative analysis, such as building height measurement, digital elevation model (DEM) construction,

and deformation monitoring, all of which require accurate 3D structure and height information.

Therefore, the aforementioned large-scale methods are challenging to apply directly to aerial remote sensing applications. We propose that while continuously mining and integrating available information, other forms of prior knowledge, such as Light Detection and Ranging (LiDAR), should be considered. The integration of LiDAR with multiview images in aerial remote sensing hardware has been increasing gradually in recent years. For instance, in 2022, Leica introduced the CityMapper [30], a hybrid urban aerial photography system that combines a five-lens oblique camera with LiDAR into a single sensor, enabling the simultaneous acquisition of multi-view images and high-density 3D LiDAR point clouds. Similarly, the Chinese carbon detection satellite, TECIS (Guomang) [31], launched in 2022, is equipped with a multi-beam laser radar and a multi-angle multi-spectral camera, capable of imaging at five different angles along its orbit. However, due to the particularity of LiDAR point cloud data topology, matching based on features and textures is difficult, and the data fusion of the two requires pixel-level alignment, which brings great challenges to data fusion.

Based on the analysis above, we propose RSGaussian, which utilizes the high-precision depth priors provided by LiDAR point clouds. First, to address the issues of Gaussian floaters and artifacts, we constrain the densification of the Gaussian distribution based on the geometric reference and the long-axis direction of the LiDAR point clouds and guide the growth and splitting of the Gaussian distribution. Second, to achieve data fusion between 3D LiDAR point clouds and 2D images and reduce measurement error, we design an alignment module that considers camera distortion, using Colmap-PCD [32] to compute the correction parameters for camera pose. Finally, to address the issue of over-stretching and further enhance the accuracy of geometric and depth estimation, we incorporate geometric structure losses (including depth, normal, and scale consistency losses) into the regularization process, to encourage the Gaussian distribution to be closer to the true depth and planar maps generated by the LiDAR points during parameter optimization.

In our experiments, we identified a notable scarcity of large-scale open datasets utilized in 3DGS that include dense LiDAR data. Therefore, we prepared a dense and comprehensive dataset ourselves, named the AIR-LONGYAN dataset. This dataset not only includes building structures but also ground and vegetation information, with each part achieving a point cloud density of 4-8 points per square meter.

Experiments have proven that our method effectively suppresses the generation of floaters in aerial remote sensing scenes, achieves photo-realistic novel view synthesis and recovers high-precision geometric structures at the same time. Moreover, the accuracy of depth estimation in our method surpasses that of other NeRF and 3DGS-based approaches.

Experiments on the open dataset UrbanScene3D and our dataset AIR-LONGYAN demonstrate that our proposed method significantly enhances the performance of 3DGS in aerial remote sensing scenarios. We have made our self-build AIR-LONGYAN dataset that integrates LiDAR and multiview images and code publicly available at https://github.com/RUME00/RSGaussian.

2. Related work

2.1. Neural Radiance Field

The Neural Radiance Field (NeRF) [11] learns the implicit representation of a 3D scene through a 5D neural network, using a multi-view image dataset and the corresponding camera poses as inputs, enabling the reconstruction of 3D scenes or the novel view synthesis via volume rendering without explicit modelling. Owing to its revolutionary neural neural-network-based implementation and realistic synthesis effects. NeRF has become a research hotspot in the fields of 3D reconstruction and novel view synthesis in computer graphics. Lots of efforts have been devoted to enhancing the photo-realistic rendering of NeRF and expanding its applicability to larger scenes. Mip-NeRF [33] proposes cone sampling in place of ray sampling and introduces Integrated Positional Encoding (IPE), significantly enhancing NeRF's detail expression accuracy across varying camera distances and reducing floaters. Building upon this, MipNeRF 360 [34] further extends the application scenario to unbounded 360° scenes. NeRF in the Wild [35] improves the network architecture to mitigate floaters caused by variable illumination and transient occluders.

Subsequent improvements for large-scale and complex scenes began to emerge: Block-NeRF [36] divides large street scene data into blocks, training and optimizing them separately, and then aligning and merging them, enabling NeRF to be applied in street-scale scenes. MegaNeRF [37] further enhances this block-wise approach with foregroundbackground separation and geometric visibility reasoning for parallel training, achieving better and faster reconstruction results in large-scale drone datasets. BungeeNeRF [38] introduces a progressive NeRF, enabling joint training at different scales, ranging from satellite level to ground level. SatNeRF [39] pioneers the application of NeRF in remote sensing photogrammetry, proposing a ray casting method based on the RPC camera model to generate meter-level digital surface models using multi-view satellite remote sensing images. LiDeNeRF [40] integrates LiDAR data into the NeRF framework to achieve decimeter-level depth estimation in first-person small-scale scenes. DS-NeRF [41] formalizes depth supervision into a loss function, leveraging sparse 3D points from SFM to constrain NeRF training, thereby improving geometry fitting accuracy with fewer input views.

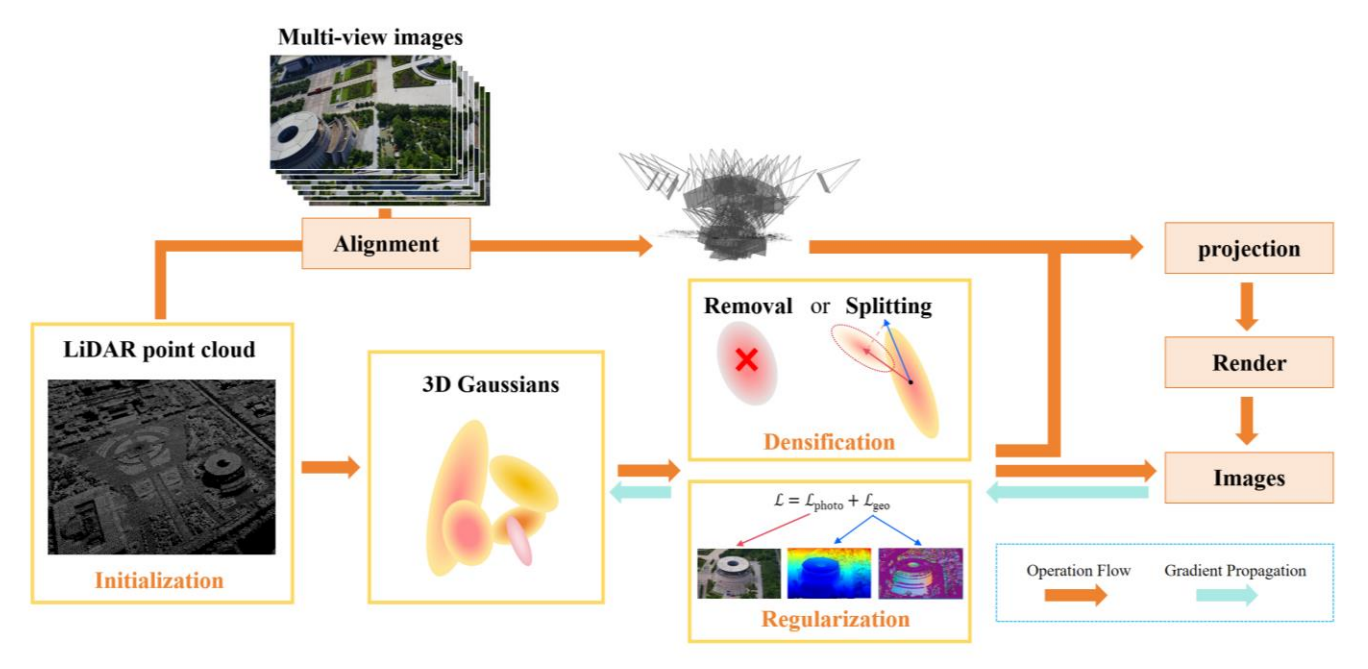


Fig. 4. Overwiew of RSGaussian.

However, despite improvements based on NeRF-related methodologies, the substantial computational and memory overhead associated with volume rendering remains a persistent challenge. Moreover, the continuous implicit representation inherently lacks the expressiveness for precise three-dimensional geometric detail, thereby inherently limiting its ability to capture fine spatial structures.

2.2. 3D Gaussian splatting

3D Gaussian splatting [12] has introduced a novel scene representation that synergizes Gaussian function and spherical harmonics, leveraging a rasterization-based rendering methodology for the synthesis of scenes derived from multiview imagery. Compared to NeRF, this method circumvents the complexities associated with ray sampling strategies and large MLP networks, achieving more realistic novel view synthesis and real-time rendering. Moreover, Gaussians scene expression adeptly represents geometric precision. However, 3DGS faced challenges in scaling to larger scenes same as NeRF. Simultaneously, 3DGS exhibits a high sensitivity to sampling frequency [17]. When the camera's focal length or the distance between the camera and the object is altered, noticeable floaters and artifacts are observed. VastGaussian [21] addresses these issues by implementing a progressive scene partitioning strategy that allocates training sets and appearance encoding for large-scale reconstruction based on drone imagery, effectively mitigating floaters occurrences. Gaussianpro [22] employs patch-matching techniques to generate normal maps and formulates a progressive Gaussian propagation strategy that guides the densification of Gaussians, thereby resolving the suboptimal reconstruction performance of 3DGS in low-texture regions due to its reliance on SFM point cloud initialization—significantly enhancing rendering quality.

Furthermore, without explicit constraints on true geometric structures, 3DGS tends to excessively proliferate split Gaussians, leading to substantial redundancy in Gaussians and memory consumption. [42] proposes a grid-based neural field for view-dependent color, and compact geometric attribute representation through vector quantization. LightGaussian [43] significantly compresses 3D Gaussian representations by over 15x, compelling the model to eliminate less contributive Gaussians. ABSgs [44] discusses the shortcomings of 3DGS regarding excessive reconstruction of high-frequency details by addressing gradient collision issues during adaptive densification processes while optimizing reconstruction outcomes at high-frequency detail areas. Gs-slam [24] employs synchronously acquired RGBD cameras as depth priors to control the densification of Gaussians, and facilitate the development of a SLAM system based on 3DGS. Pixel-gs [23] addresses the issues of blurring and needle-like artifacts that arise in regions with insufficient initial points. This artifact is attributed to the Gaussians densification strategy that only considers the average gradient magnitude of points from observable viewpoints. The paper introduces a dynamic scaling of the gradient field based on the distance from the scene to the camera, aiming to suppress the growth of floaters near the camera.

3. Method

The overview structure of our method is shown in **Fig. 4**. In **Section 3.1**, we introduce a densification strategy with LiDAR point cloud as geometric constraints. The LiDAR point clouds constrain the densification of the Gaussians, guiding the growth and splitting of Gaussians. In **Section 3.2**, we design a fusion module to achieve pixel-level alignment between LiDAR point clouds and multi-view images

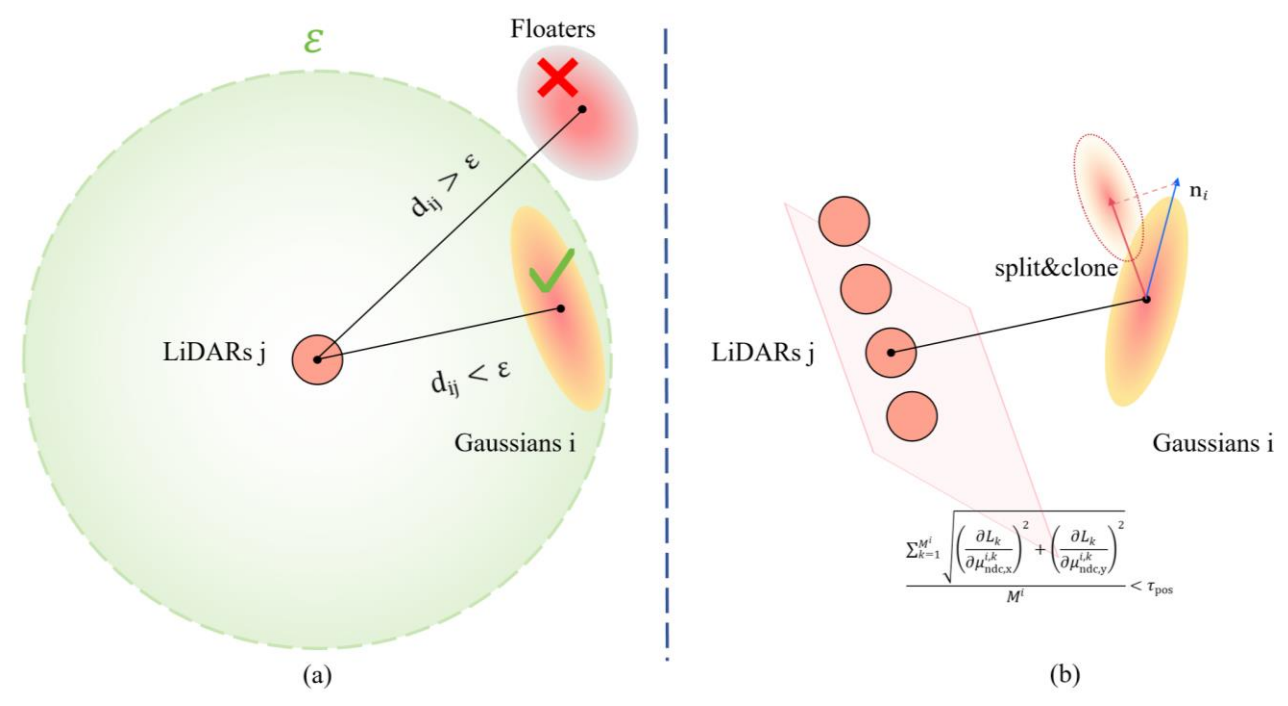


Fig. 5. Gaussians densification strategy. (a)Removal of redundant Gaussians, (b)Splitting of under-reconstructed Gaussians .

unifying the fused scene under the WGS84 ECEF geodetic coordinate system. This enables the model to acquire real coordinates and scale while expanding the camera model parameters from a simple pinhole camera model to distorted camera model to reduce biases caused by camera distortion. Finally, in **Section 3.3**, we design a geometric loss in the regularization section, incorporating 2D depth maps and normal maps derived from the projection of LiDAR point clouds into the loss function. This aids in optimizing the parameters of the 3DGS to better align with real depth and planes, enhancing the accuracy of the model's depth estimation.

Define the set of aerial aerial remote sensing multi-view images as $\mathcal{I} = \{l_i \mid i=1 \dots N_I\}$, and the LiDAR point cloud as $\mathcal{L} = \{l_m \mid m=1 \dots N_L\}$, where $l_m \in \mathbb{R}^3$ is the 3D coordinates of the point cloud in the world coordinate system. Let $\mathcal{F}^i = \{x_j^i \mid j=1 \dots N_{F_i}\}$ be the set of feature points extracted from the image I_i , where each feature point is represented by its two-dimensional coordinates $x_j^i \in \mathbb{R}^2$ in the pixel coordinate system. Let $\mathcal{S} = \{(G_m, \alpha, \Sigma_{3D}^m, c \mid m=1 \dots N_S\}$ be the set of reconstructed 3D Gaussians, where each Gaussians is characterized by its coordinates $G_m \in \mathbb{R}^3$ in the world coordinate system, its opacity α , the 3×3 covariance matrix $\Sigma_{3D}^m = R_m S_m S_m^T R_m^T$ that describes the rotation R_m and scaling S_m of the Gaussian ellipsoid's three axes, and the color c modeled by spherical harmonics.

3.1. Gaussians Densification Strategy Guided by LiDAR Point Cloud

To address the generation of numerous floaters and artifacts with inaccurate depth estimation in regions where the input views are sparse, we aim to improve the densification strategy by leveraging the depth prior provided by LiDAR. LiDAR uses

laser diodes to emit short pulsed laser beams, which possess high directionality, monochromaticity, and coherence, allowing them to measure distances with extremely high precision, thereby offering high-precision depth information and a robust geometric framework [45]. Based on this, we direct the Gaussians to grow along the direction obtained by projecting their long axis onto the local tangent plane of the LiDAR point cloud [46].

Our densification strategy consists of two parts: determining redundant Gaussians for removal and determining underreconstructed Gaussians for splitting, while guiding the splitting direction.

3.1.1. Removal of redundant Gaussians

By initializing with the original LiDAR point cloud, and at regular intervals defined by a specified number of iterations in the original densification strategy, we employ a Kd-tree [47] nearest neighbor search of Euclidean distance to find the nearest LiDAR point $l_j = (\mu_{w,x}^j, \mu_{w,y}^j, \mu_{w,z}^j)$, to Gaussians $G_i = (\mu_{w,x}^i, \mu_{w,y}^i, \mu_{w,z}^i)$ in the world coordinate system. If the smallest distance among these points remains greater than a set distance threshold as:

$$d_{ij} = \|G_i - l_j\|_2 \operatorname{argmin}(d_{ij}) >$$
 (1)

Indicating that the existing Gaussians have deviated from the correct geometric structure, or if the opacity of the Gaussian point is below a certain threshold $\alpha_i < \epsilon$, signifying that the contribution of the Gaussians is too small, we then delete the current Gaussians.

3.1.2. Splitting of under-reconstructed Gaussians

When determining which Gaussians under reconstruction, we simultaneously calculate the NDC (Normalized Device Coordinate) coordinates $(\mu_{ndc,x}^{i,k}, \mu_{ndc,y}^{i,k}, \mu_{ndc,z}^{i,k})$ of the current Gaussians i under the perspective k, and for all visible perspectives M^i participating in the calculation, we average the gradients of the loss function L_k response used in PixelGS [23]. When it is less than the set threshold, as in Eq.2, the existing Gaussians are considered inadequate in fully representing the scene and require densification.

$$\frac{\sum_{k=1}^{M^{i}} m_{k}^{i} \times \sqrt{\left(\frac{\partial L_{k}}{\partial \mu_{\text{ncc,x}}^{2}}\right)^{2} + \left(\frac{\partial L_{k}}{\partial \mu_{\text{ndc,y}}^{k}}\right)^{2}}}{\sum_{k=1}^{M^{i}} m_{k}^{i}} > \tau_{\text{pos}}$$
 (2)

As an ellipsoid structure expressed by the covariance matrix, the maximum component of eigenvectors of Gaussians function can be considered as the long axis of the Gaussians and can be expressed as:

$$n_i = R_i[r,:], r = argmax([s_1, s_2, s_3])$$
 (3)

The newly generated Gaussians will grow along the direction obtained by projecting n_i onto the local tangent plane of the LiDAR point cloud, as shown in **Fig. 5** and **Eq.4**:

$$n_{i+} = n_i - \frac{n_i \cdot N}{N \cdot N} N \tag{4}$$

Where N is the local normal plane of the LiDAR point cloud. Our approach not only fully utilizes the high-precision geometric information from the LiDAR point cloud but also provides a more rational densification direction for Gaussian distributions in 3DGS. Consequently, it effectively alleviates depth errors caused by sparse view angles and insufficient geometric perception.

3.2. Precision Alignment of LiDAR Point Cloud and Multi-View Images

The application of the method in **section 3.1** requires that the 2D multi-view images and the 3D LiDAR point cloud should be precisely aligned. This is particularly challenging for LiDAR data, as it lacks texture features that make direct matching difficult. Direct projection errors can reach dozens of pixels, resulting in poor performance of the synthesis results, especially in areas where height changes dramatically and image distortion edges are evident. This phenomenon is verified in the experiment designed in **Section 4.2.3.2**.

To achieve this, we have designed a registration module to achieve pixel-level alignment between LiDAR point clouds and feature points extracted from a 2D image set. Firstly, we use the camera pose provided by the integrated navigation system, which combines onboard differential positioning components (DGPS) and inertial measurement units (IMU), as the initial value, offering centimeter-level accuracy [48]. We

project both the images and the extracted feature points from the camera coordinate system into the world coordinate system.

Secondly, we introduce a distorted camera model based on the Brown–Conrady [43] model that incorporates the coefficients of the second- and fourth-order terms k_1 , k_2 of radial distortion to accurately describe the optical distortion characteristics of the lens and correct for such distortion. It is capable of calculating radial components by utilizing an even-order polynomial [50], restoring the images to their true geometric relationships.

Let (u', v') represent the ideal image coordinates without distortion, (u, v) represent the actual image coordinates, (u_0, v_0) represent the image coordinates of the optical axis center, and r represent the distance from the image point to the reference point:

$$r = \sqrt{(u' - u_0)^2 + (v' - v_0)^2}$$
 (5)

Let k_1 and k_2 be the second-order and fourth-order distortion coefficients in the respective directions u and v. The radial distortion model considering fourth-order lens distortion is given by:

$$u' = u_0 + (u - u_0) \cdot (1 + k_1 \cdot r^2 + k_2 \cdot r^4)$$

$$v' = v_0 + (v - v_0) \cdot (1 + k_1 \cdot r^2 + k_2 \cdot r^4)$$
(6)

Therefore, we express the transformation relationship between the pixel coordinate system and the world coordinate system through the fourth-order radial distortion camera model as follows:

$$Z \begin{bmatrix} u \\ v \\ 1 \end{bmatrix} = \begin{bmatrix} 1 + k_1 r^2 + k_2 r^4 & 0 & 0 \\ 0 & 1 + k_1 r^2 + k_2 r^4 & 0 \\ 0 & 0 & 1 \end{bmatrix} \times \begin{bmatrix} \alpha_x & 0 & u_0 \\ 0 & \alpha_y & v_0 \\ 0 & 0 & 1 \end{bmatrix} \\ \times \begin{bmatrix} f_x & 0 & 0 & 0 \\ 0 & f_y & 0 & 0 \\ 0 & 0 & 1 & 0 \end{bmatrix} \begin{bmatrix} R & t \\ 0^T & 1 \end{bmatrix} \begin{bmatrix} x_w \\ y_w \\ z_w \\ 1 \end{bmatrix} - \begin{bmatrix} u_0 (k_1 r^2 + k_2 r^4) \\ v_0 (k_1 r^2 + k_2 r^4) \end{bmatrix}$$
(7)

Where α_x , α_y denotes the physical dimensions of each pixel in the u-axis and v-axis directions, after rearranging, we get:

$$Zl_{uv} = D_1K(Rl_m + t) - D_2$$
 (8)

In this context, Z represents the depth value of the optical center, utilized for the normalization of homogeneous coordinates. $l_{uv} = \begin{bmatrix} u \\ v \end{bmatrix}$ denotes the pixel coordinates in the

image coordinate system, while
$$l_m = \begin{bmatrix} x_w \\ y_w \\ z_w \end{bmatrix}$$
 stands for the

coordinates of points in the LiDAR point cloud \mathcal{L} within the world coordinate system. D_1 , D_2 are distortion matrices, and K denotes the intrinsic matrix of the camera model. Both the distortion parameters and the intrinsic parameters are provided by the camera calibration file. R and t represent the rotation matrix and translation matrix, respectively, which define the camera's pose. These matrices are initialized using the combined navigation solution provided by the onboard differential positioning element and inertial measurement unit

(IMU). In **Eq.7**, the feature point coordinates and LiDAR point cloud coordinates are treated as fixed values, serving as inputs for the optimization process to estimate the camera's pose accurately.

Finally, we employ the Colmap-PCD [32] algorithm framework for the solution process, wherein the LiDAR point cloud is projected onto the known camera imaging plane by Eq.8. Colmap-PCD[25] employs three progressive bundle adjustment methods for calculating the optimal estimation of camera poses, incorporating 2D features, image poses, and LiDAR points into a factor graph for optimization. The LiDAR point cloud is divided into fixed-size voxels, and a quadrilateral pyramid is formed through four lines [32]. By traversing the LiDAR points within the voxel, for each LiDAR point l_m in the \mathcal{L} , we transform its coordinates from the world coordinate system to the camera coordinate system. Subsequently, we project it onto the imaging plane to obtain its corresponding pixel coordinates in the image l_{uv} , typically represented by multiple pixels. If the feature point x_i^i in the image I_i falls within this range, we regard it as the LiDAR reference point corresponding to the feature point. When multiple LiDAR reference points correspond to a single feature point, we select the one with the smallest distance.

By minimizing the reprojection error, the optimal estimation of camera poses is solved, thereby achieving pixel-level alignment of LiDAR point clouds and multi-view images in the world coordinate system.

3.3. Geometric Consistency Constraint

To address the issue of over-stretching and further enhance the accuracy of geometric and depth estimation, we introduce a geometric consistency constraint. This constraint will be incorporated into the regularization process of Gaussians parameter optimization, utilizing depth maps and normal maps generated from LiDAR point clouds as geometric consistency constraints, which encourage the Gaussians to better conform to the true geometric shape, thereby improving the accuracy and reliability of synthesis results.

Firstly, considering the resolution of the LiDAR point cloud obtained from aerial remote sensing is relatively low compared to the image resolution, making it infeasible to directly generate dense depth and normal maps, we employ PatchMatch Stereo [51] as a framework to propagate the sparse point cloud and generate dense depth and normal maps. These dense maps are subsequently used to compute the depth and normal residuals between the rendered images and the real images, which are then adjusted through backpropagation optimization.

The geometric consistency constraint consists of three components: depth constraint, normal constraint, and scale constraint.

$$\mathcal{L}_{geo} = \alpha \mathcal{L}_{depth} + \beta \mathcal{L}_{normal} + \gamma \mathcal{L}_{scale}$$
 (9)

We represent the depth map and normal map generated from the LiDAR point cloud as the longitudinal direction and planar direction of the scene:

$$\mathcal{L}_{\text{depth}} = \sum_{p \in \mathcal{O}} \| \hat{D}(p) - \bar{D}(p) \|_{1} + \| 1 - \hat{D}(p)^{\mathsf{T}} \bar{D}(p) \|_{1}$$
(10)

$$\mathcal{L}_{\text{normal}} = \sum_{p \in \mathcal{O}} \| \hat{N}(p) - \bar{N}(p) \|_{1} + \| 1 - \hat{N}(p)^{\mathsf{T}} \bar{N}(p) \|_{1}$$
(11)

The scale regularization loss ensures that the shortest axis of the Gaussians can represent the normal direction, thus restricting the minimum scale of the Gaussian distribution to approach zero, effectively suppressing excessive inflation of Gaussians [22].

Ultimately, the geometric constraint can be expressed as a weighted sum of three loss terms, and the overall loss function combines both photometric and geometric losses:

$$\mathcal{L}_{\text{photo}} = (1 - \lambda)\mathcal{L}_1 + \lambda \mathcal{L}_{\text{D-SSIM}}$$
 (12)

$$\mathcal{L} = \mathcal{L}_{\text{photo}} + \mathcal{L}_{\text{geo}} \tag{13}$$

Among these, α , β , γ and λ are all hyperparameters. The Structural Similarity Index (SSIM) loss is quantified, denoted as $\mathcal{L}_{\text{D-SSIM}}$. Here, \hat{D} represents the depth map rendered from the image, \bar{D} represents the depth map generated by the LiDAR point cloud, \hat{N} represents the normal map rendered from the image, and \bar{N} represents the normal map generated by the LiDAR point cloud. The subscript p denotes the current pixel, and \mathcal{O} denotes the set of all valid pixels. This approach not only enhances the accuracy of the reconstruction results but also improves the adaptability and robustness of 3DGS in complex scenes.

4. Experiment

4.1. Datasets and Implementation Details

4.1.1. Datasets

We conducted comparative experiments on both an open dataset and a self-built dataset AIR-LONGYAN. For the open dataset, we selected the Science and Art Building scene from the large-scale urban dataset UrbanScene3D [52].

UrbanScene3D

UrbanScene3D(UR3D) contains thousands of images under 128k high-resolution covering 16 scenes including largescale urban regions with 136 areas in total and provides building point clouds acquired by LiDAR scanners.

The LiDAR scanner is Trimble X7 with self-calibration and self-registration techniques. The ranging noise is 0.5mm, the ranging accuracy is 2mm, and the angular accuracy is 21". The accuracy of 3D points is 1.5mm at 10m and 2.4mm at 20m [52], in the scene we use, ArtSci, the overall error of registration is 3mm. The point cloud density can reach 0.1-0.3 pts.

It is important to note that UrbanScene3D offers datasets collected along various paths. As our focus is primarily on applications of aerial remote sensing, we chose the dataset collected under the oblique photogrammetric path.

It has been used in MegaNeRF [37] and VastGaussian [21], but due to its relatively low LiDAR point cloud density and limited LiDAR content to only the architectural parts, we have also established our own dataset.

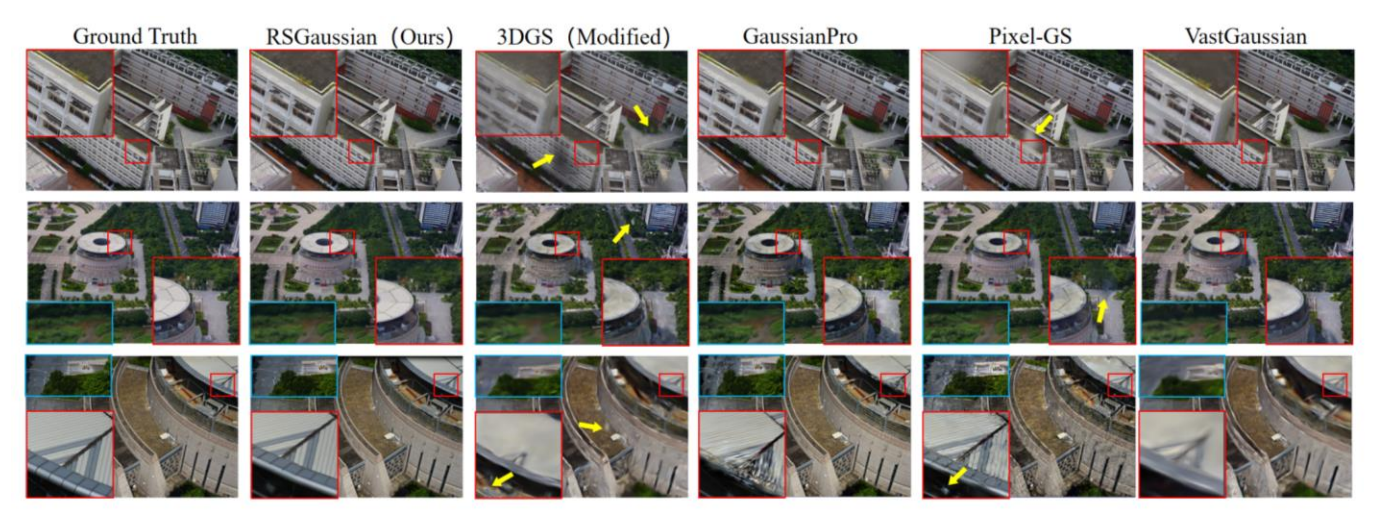


Fig. 6. Novel view synthesis results between RSGaussian and previous work.

AIR-LONGYAN

In the AIR-LONGYAN dataset, we utilized a DJI m300 drone equipped with a high-resolution five-camera array to collect multi-view stereo images of an area of about 25 in Longvan City, Fujian Province, following an oblique photogrammetric path. The target area contains buildings, vegetation, roads, and ground. The dataset comprises 602 images, characterized by a spatial resolution that attains 0.1 meters. the LiDAR payload was the Riegl VQ580-II, designed for a repetition frequency of 150 kHz, with a maximum echo recording capability of over ten single pulses. The theoretical point cloud density per flight line was 3.6 pts, with an overlap rate greater than 67%, resulting in an actual point cloud density of 4-8 pts after three coverage flights. The matching accuracy between flight lines was better than 0.2 meters, and the geometric positioning accuracy was better than 1 meter. Each photo is accompanied by the initial camera pose provided by the integrated navigation of the onboard Differential Global Positioning System (DGPS) and Inertial Measurement Unit (IMU), as well as calibrated camera intrinsic parameters. Additionally, control points collected by GNSS RTK equipment were also provided.

4.1.2. Implementation Details

Our approach is grounded in the widely recognized open-source baseline of 3DGS. Analogous to the training protocol detailed in 3DGS, our model underwent 30,000 iterations across all scenes, adhering to the same training schedule and hyperparameters as 3DGS. Beyond the original cloning and splitting Gaussian densification strategy employed in 3DGS, we integrated the novel densification strategy introduced in this study, executing it every 50 training iterations. The distance threshold σ was configured to 2m. Regarding our loss function parameters, we set α = 100, β = 0.001, γ = 0.001, λ = 0.2, in alignment with the settings used in 3DGS. All experiments were conducted on an RTX A6000 GPU. In all datasets, we use 70% of the data for the training set, 15% for the validation set, and 15% for the testing set.

We compared our method with the original 3DGS [12], VastGaussian [21], Gaussianpro [22] and Pixel-GS [23]. To evaluate the performance of novel view synthesis, we applied four widely used metrics: Peak Signal-to-Noise Ratio (PSNR), Structural Similarity (SSIM), and Learned Perceptual Image Patch Similarity (LPIPS). Additionally, we introduced the Root Mean Square Error (LiDAR RMSE) of LiDAR points across the entire scene as an evaluation metric to measure the geometric accuracy of our method.

4.2. Results and discussion

4.2.1. Visual Result Analysis

As Fig. 6 shows, the floaters are indicated by yellow arrows, the architectural texture details are enlarged by the red box, and the vegetative details are enlarged by the blue box. It can be seen that the original 3DGS produces floaters and artifacts, performing poorly in both vegetation and architectural texture details; GaussianPro's densification improvement in underreconstructed areas allows the model to initially restore texture details, but it still lacks clarity; Pixel-GS, due to the targeted improvements made, reduces the phenomenon of needle-like over-stretching, making the vegetative details and architectural textures clearer, but it does not consider the suppression of floaters; VastGaussian, which uses block training to suppress the generation of floaters in large scenes, also lacks clarity and produces an overall blurry synthesized image.

In contrast, our method further resolves this issue by effectively suppressing floaters and achieving clearer images of the building structures of interest. This improvement is primarily due to the accurate geometry information provided by dense LiDAR point clouds. Additionally, our Gaussian point density control strategy encourages the growth of Gaussians along actual geometric reference, and our camera model also corrects image edge distortions, thereby reducing scale distortions in the images.

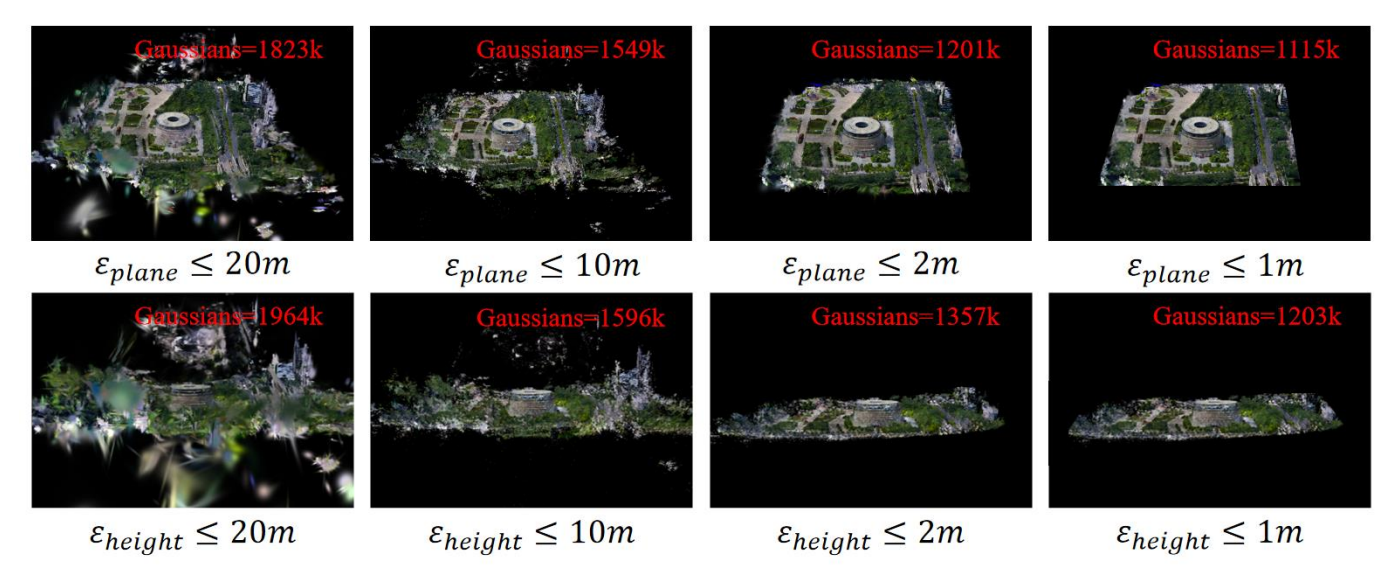


Fig. 7. The effect of setting different distance thresholds in densification strategies on the distribution of Gaussians (the number of Gaussians in the scene is marked in red).

Table 1
Quantitative comparisons of our method compared to previous work on UR3D and AIR-LONGYAN datasets. The best results are highlighted and the second results are underlined.

Dataset		U	R3D(Artsci)	•	AIR	R-LONGYA	AN
Metrics	PSNR↑	SSIM↑	LPIPS↓	LiDAR RMSE↓	PSNR↑	SSIM↑	LPIPS↓	LiDAR RMSE↓
3DGS	21.048	0.528	0.623	8.547	21.034	0.534	0.619	8.144
VastGaussian	22.901	0.689	0.525	8.429	22.942	0.676	0.569	8.813
Pixel-GS	24.026	0.765	0.394	7.432	24.639	0.783	0.337	6.837
GaussianPro	25.910	0.785	0.106	<u>5.142</u>	25.722	0.823	0.204	<u>4.216</u>
RSGaussian(Ours)	26.747	0.876	0.108	0.283	26.908	0.858	0.192	0.137

4.2.2. Precision Metrics Analysis

Table 1 demonstrates that our method achieves the best performance in PSNR, SSIM and LiDAR RMSE on the UrbanScene3Dopen dataset, particularly excelling in depth estimation accuracy. Our method slightly lags behind GaussianPro in LPIPS by only 0.002. On our self-built AIR-LONGYAN dataset, our method attains the best performance in PSNR, SSIM, LPIPS, and LiDAR RMSE, particularly excelling in depth estimation accuracy. Additionally, as shown in Fig. 8, indicated by the yellow frame, the coordinate accuracy of control points reaches the decimeter level (ground truth provided by GNSS RTK devices). It is noted that the better performance on the self-built dataset may be related to the denser point clouds serving as constraints, a point we will delve into further in the ablation study in Section 4.2.5.

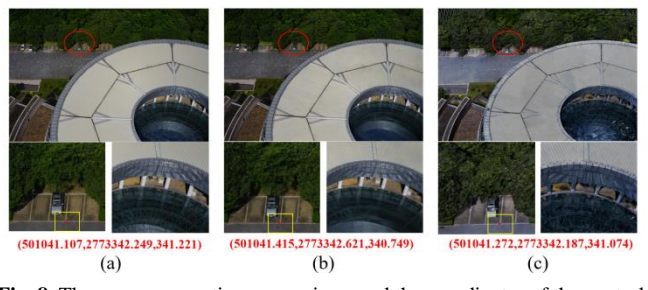


Fig. 8. The same perspective comparison, and the coordinates of the control points. (a)Ground truth, (b)RSGaussian(Ours), (c)Oblique photogrammetry.

4.2.3. Ablation Study

We performed an ablation analysis on the AIR-LONGYAN dataset to assess the impact of each component in the RSGaussian model as **Table 2** shows.

Table 2
Ablation on distorted camera modelling, LiDAR constraint and geometric loss constraint.

Model setting	PSNR↑	SSIM↑	LPIPS↓	LiDAR RMSE↓
w/o LiDARconst	24.661	0.726	0.346	4.469
w/o Alignment	20.424	0.627	0.402	0.523
w/o depthloss	26.026	0.749	0.214	1.432
Full model	26.908	0.858	0.192	0.137

4.2.3.1. LiDARconst: The effectiveness of our densification strategy

To explore the efficacy of our densification strategy applied to 3D Gaussian distributions bound by LiDAR point clouds, we undertook experiments on the AIR-LONGYAN dataset, as illustrated in **Table 2** (first row). Our densification strategy notably augmented various metrics, enhancing both visual quality and the precision of depth estimation. This enhancement is ascribed to the high-accuracy geometric directives furnished by the LiDAR point clouds. Throughout the densification process, the proliferation and division of

Gaussians were meticulously contained within the LiDAR point cloud framework, thereby effectively alleviating problems such as floaters artifacts and overzealous splitting of Gaussians.

To investigate the influence of the Gaussians growth mechanism and the configuration of LiDAR point cloud distance thresholds in the densification strategy on experimental outcomes, we established horizontal and vertical distance thresholds of 1 meter, 2 meters, 10 meters, and 20 meters.

As illustrated in **Fig. 7**, the setting of the distance threshold notably impacted the Gaussian distribution. With a progressive decrease in this threshold, the constraints imposed on the splitting and expansion of Gaussians intensified, eventually leading to the convergence of all Gaussians within the LiDAR framework. The total number of Gaussians within the scene (indicated in red) also decreased correspondingly, thereby reducing the overall number of Gaussians that required optimization. Furthermore, the integration of Gaussian parameter optimization with LiDAR data facilitated the acceleration of the optimization process, enhanced training efficiency, and minimized memory demands (as evidenced in **Table 3**). Although a further reduction in the threshold might theoretically yield numerically superior geometric accuracy, given the geometric positioning accuracy of LiDAR point clouds is 1 meter, a threshold reduction beyond this point would not yield any practical improvement in geometric accuracy. Consequently, we adopted a 1-meter threshold in our final densification strategy.

Table 3Training Time and Resource Consumption Under Different Distance Thresholds

Istance Timesi	10145			
Thresholds	PSNR↑	Gaussians	Training	VRAM
20m	24.021	1823k	2h03min	3.49G
10m	25.185	1549k	1h47min	4.469
2m	26.247	1201k	1h28min	1.82G
1m	26.908	1115K	56min	1.67G

4.2.3.2. Alignment: The Necessity of Precise Alignment

This section aims to elucidate the critical importance of the meticulously devised LiDAR and multi-view images precise alignment scheme discussed previously. As indicated in the second row of **Table 2**, employing solely the LiDAR data postglobal orientation as an initialization point for constraining Gaussians densification without the incorporation of precise alignment results in a significant reduction in the PSNR of novel view synthesis during training. This phenomenon arises because even minor alignment errors within a few pixels can lead to a complete distortion of depth information, thereby causing disorder in the growth and splitting of Gaussians. This disorder is particularly pronounced in areas with significant height variations, as illustrated in Fig. 9, the sculpture at the center of the plaza (marked by a red box) exhibits notable depth changes. Any slight misalignment in these areas would yield severely distorted reconstruction results.



Fig. 9. Comparison of precise alignment modules in novel view synthesis. (a) with Alignment, (b) w/o Alignment.

4.2.3.3. Depthloss: Geometric Consistency Constraint

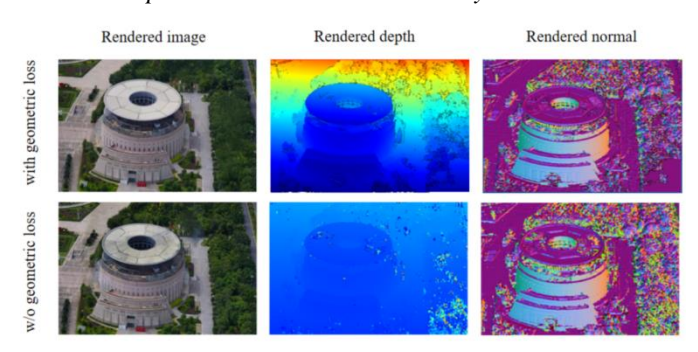


Fig. 10. The influence of geometric consistency loss constraints on rendered images, depth maps, and normal maps. (Distance)

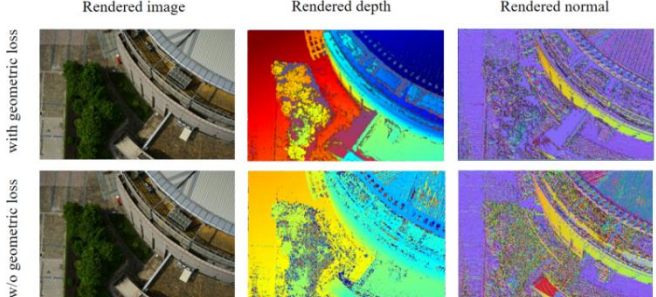


Fig. 11. The influence of geometric consistency loss constraints on rendered images, depth maps, and normal maps. (Close)

To investigate the effectiveness of our geometric consistency loss, we conducted experiments on the AIR-LONGYAN dataset, as shown in Table 2 (third row). The original loss function exclusively considered photometric losses (L1 loss and SSIM loss), prioritizing visual appearance. By incorporating depth and plane consistency losses into the loss function, we achieved enhanced accuracy in depth estimation while maintaining superior visual quality. Fig. 10 and Fig. 11 respectively illustrate the effects of geometric loss constraints on distance-range and close-range training results. As depicted, incorporating the geometric loss into the loss function only slightly improves the visual quality of the rendered image. However, the introduction of geometric losses notably improved the geometric precision of the rendered depth maps and normal maps. This improvement is particularly evident in large-scale distant view, where rendered depth maps without geometric loss constraints almost fail to express depth differentiation and exhibit substantial noise in vegetated areas.

4.2.4. Analysis of Floaters Elimination Based on

Gaussians Tri-View

Our method effectively inhibits the generation of floaters while providing greater clarity at the focal areas of the building. This is primarily due to the more accurate depths provided by LiDAR point clouds compared to those extracted by image algorithms from sparse point clouds. Additionally, our Gaussians densification strategy encourages Gaussians to grow along the true surface. To further demonstrate the constraints imposed by our method on floaters, we generated three-view depth distribution maps (set all opacity to 1, scale to 1) of Gaussians created by 3DGS and our method, as shown in Fig. 12. The 3DGS method actually generates a much larger quantity of floaters than expected within the scene, whereas our method effectively constrains these floaters within the true geometric framework.

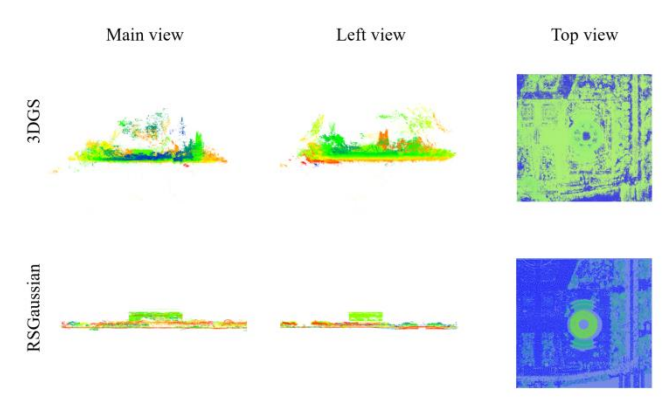


Fig. 12. RSGaussian and 3DGS generate three-view distribution of Gaussians positions for the entire scene.

4.2.5. Analysis of the Impact of LiDAR Point Cloud Density

The performance discrepancy observed between the UrbanScene3Ddataset and the AIR-LONGYAN dataset is likely attributable to the higher density of LiDAR point clouds in the AIR-LONGYAN dataset, as illustrated in Fig. 13. Notably, the point cloud density in the AIR-LONGYAN dataset significantly exceeds that in the UrbanScene3D dataset, which only includes point clouds of building portions. Consequently, this section will investigate the impact of LiDAR point cloud density on our method. To this end, we conducted an ablation study by repeatedly downsampling the LiDAR point clouds in the AIR-LONGYAN dataset to obtain point clouds at densities of 5%, 25%, 50%, and 75%, which served as constraints for the Gaussians densification strategy. The results, presented in **Table 4**, demonstrate that point cloud density significantly influences the quality of novel view synthesis. There is a marked improvement in the quality of synthesized images with increasing point cloud density, peaking at the highest density. Additionally, it is noteworthy that the enhancement in LiDAR RMSE is more pronounced than in the other three metrics as point cloud density increases. This observation aligns with the findings of [53].

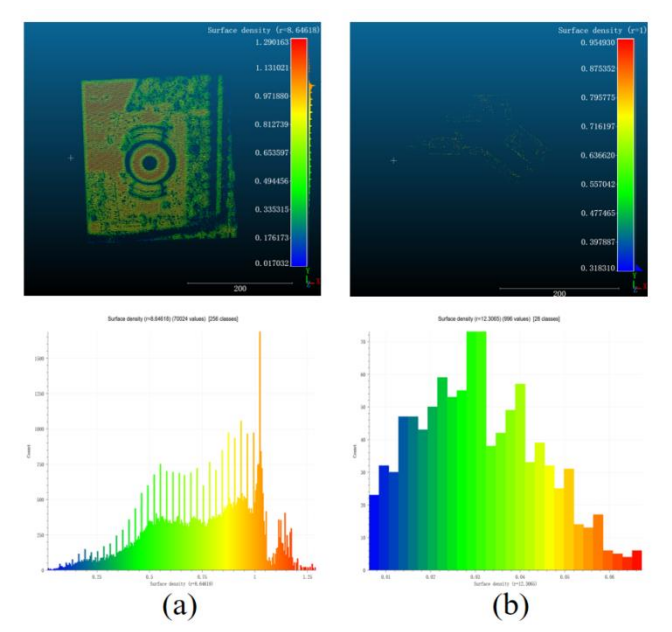


Fig. 13. The LiDAR point cloud density maps. (a) AIR-LONGYAN dataset, (b) UrbanScene3D dataset.

Table 4The impact of different point cloud densities on training results.

Piont Cloud Density	PSNR↑	SSIM↑	LPIPS↓	LiDAR RMSE↓
10%	26.304	0.817	0.234	0.214
25%	26.419	0.821	0.227	0.198
50%	26.587	0.836	0.214	0.174
75%	26.725	0.844	0.202	0.158
Dense	26.908	0.858	0.192	0.137

5. Conclusion

This study introduces RSGaussian, a novel view synthesis method for aerial remote sensing that leverages LiDAR point cloud as a constraint. Our approach not only achieves realistic novel view synthesis in large-scale aerial remote sensing scenes but also recovers high-precision geometric structures which is essential for remote sensing. Firstly, our method incorporates LiDAR point clouds as constraints for Gaussian point densification, guiding the growth and splitting of Gaussians along the geometric benchmarks provided by LiDAR point clouds. This addresses the issue of floaters existing in aerial remote sensing scenes, thereby enhancing the visual quality of synthesized views. Secondly, the method derives coordinate transformations including distortion parameters for camera models to achieve pixel-level alignment between LiDAR point clouds and 2D images, enabling the fusion of heterogeneous data and high-precision geoalignment. Finally, our approach integrates depth and plane consistency losses into the regularization process, encouraging Gaussians to align closer to the real depth and plane representations, which significantly improves the geometric estimation accuracy of the model. Experiments demonstrate that our method excels in various visual quality metrics and substantially enhances geometric precision in depth estimation, balancing the visual appeal of 3DGS with the geometric accuracy of LiDAR.

However, the application of satellite-borne aerial remote sensing data still requires further work for improvement. Satellite-borne aerial remote sensing data have higher orbits and greater distances, making the LiDAR point cloud sparser and the multi-view images angles fewer, which presents a challenging task. In the future, corresponding improvements in satellite-borne aerial remote sensing will be considered in our methods

References

- [1] Aicardi, I., Chiabrando, F., Grasso, N., Lingua, A. M., Noardo, F., & Spanò, A. (2016). UAV photogrammetry with oblique images: First analysis on data acquisition and processing. The International Archives of the Photogrammetry, aerial remote sensing and Spatial Information Sciences, 41, 835-842.
- [2] F. Remondino and M. Gerke, (2015, September). Oblique aerial images– a review. In Photogrammetric week (Vol. 15, No. 12, pp. 75-81).
- [3] Wu, B., Xie, L., Hu, H., Zhu, Q., & Yau, E. (2018). Integration of aerial oblique images and terrestrial images for optimized 3D modeling in urban areas. ISPRS journal of photogrammetry and aerial remote sensing, 139, 119-132
- [4] J. L. Schonberger and J. M. Frahm, (2016). Structure-from-motion revisited. In Proceedings of the IEEE conference on computer vision and pattern recognition (pp. 4104-4113).
- [5] Y. Yao, Z. Luo, S. Li, T. Fang, and L. Quan, (2018). Mysnet: Depth inference for unstructured multi-view stereo. In Proceedings of the European conference on computer vision (ECCV) (pp. 767-783). DOI: 10.1007/978-3-030-01237-3_47
- [6] Agarwal, S., Snavely, N., Seitz, S. M., & Szeliski, R. (2010). Bundle adjustment in the large. In Lecture Notes in Computer Science (pp. 29– 42). Springer Berlin Heidelberg. https://doi.org/10.1007/978-3-642-15552-9_3
- [7] Svennevig, K., Guarnieri, P., & Stemmerik, L. (2015). From oblique photogrammetry to a 3D model – Structural modeling of Kilen, eastern North Greenland. Computers & Description of Kilen, eastern https://doi.org/10.1016/j.cageo.2015.07.008
- [8] Grammatikopoulos, L., Kalisperakis, I., Karras, G.E., & Petsa, E. (2007). AUTOMATIC MULTIVIEW TEXTURE MAPPING OF 3 D SURFACE PROJECTIONS.
- [9] Kuznetsov, A., Wang, X., Mullia, K., Luan, F., Xu, Z., Hašan, M., & Ramamoorthi, R. (2022). Rendering Neural Materials on Curved Surfaces. ACM SIGGRAPH 2022 Conference Proceedings.
- [10] M. Botsch, M. Pauly, C. Rossl, S. Bischoff, and L. Kobbelt, (2006). Geometric modeling based on triangle meshes. In ACM SIGGRAPH 2006 Courses (pp. 1-es). DOI: 10.1145/1185657.1185839
- [11] Mildenhall, B., Srinivasan, P. P., Tancik, M., Barron, J. T., Ramamoorthi, R., & Ng, R. (2021). NeRF. Communications of the ACM, 65(1), 99–106. https://doi.org/10.1145/3503250
- [12]Kerbl, B., Kopanas, G., Leimkuehler, T., & Drettakis, G. (2023). 3D gaussian splatting for real-time radiance field rendering. ACM Transactions on Graphics, 42(4), 1–14. https://doi.org/10.1145/3592433
- [13] Müller, T., Evans, A., Schied, C., & Keller, A. (2022). Instant neural graphics primitives with a multiresolution hash encoding. ACM transactions on graphics (TOG), 41(4), 1-15. DOI: 10.1145/3528223.3530127
- [14]J. T. Barron, B. Mildenhall, D. Verbin, P. P. Srinivasan, and P. Hedman, (2023). Zip-nerf: Anti-aliased grid-based neural radiance fields. In Proceedings of the IEEE/CVF International Conference on Computer Vision (pp. 19697-19705).
- [15]A. Chen, Z. Xu, A. Geiger, J. Yu, and H. Su, (2022, October). Tensorf: Tensorial radiance fields. In European conference on computer vision (pp. 333-350). Cham: Springer Nature Switzerland.
- [16]Q. Xu, Z. Xu, J. Philip, S. Bi, Z. Shu, K. Sunkavalli, et al., (2022). Point-nerf: Point-based neural radiance fields. In Proceedings of the IEEE/CVF conference on computer vision and pattern recognition (pp. 5438-5448).
- [17]Yu, Z., Chen, A., Huang, B., Sattler, T., & Geiger, A. (2024). Mip-Splatting: Alias-Free 3D gaussian splatting. 2024 IEEE/CVF Conference on Computer Vision and Pattern Recognition (CVPR), 19447–19456. https://doi.org/10.1109/cvpr52733.2024.01839
- [18] Yan, Z., Low, W. F., Chen, Y., & Lee, G. H. (2024). Multi-Scale 3D gaussian splatting for anti-aliased rendering. 2024 IEEE/CVF Conference

- on Computer Vision and Pattern Recognition (CVPR), 20923–20931. https://doi.org/10.1109/cvpr52733.2024.01977
- [19]Liang, Z., Zhang, Q., Hu, W., Zhu, L., Feng, Y., & Jia, K. (2024). Analytic-Splatting: Anti-Aliased 3D Gaussian Splatting via Analytic Integration. In Lecture Notes in Computer Science (pp. 281–297). Springer Nature Switzerland. https://doi.org/10.1007/978-3-031-72643-9-17
- [20] Lu, T., Yu, M., Xu, L., Xiangli, Y., Wang, L., Lin, D., & Dai, B. (2024). Scaffold-GS: Structured 3D gaussians for view-adaptive rendering. 2024 IEEE/CVF Conference on Computer Vision and Pattern Recognition (CVPR), 20654–20664. https://doi.org/10.1109/cvpr52733.2024.01952
- [21]J. Lin, Z. Li, X. Tang, J. Liu, S. Liu, J. Liu, et al., (2024). Vastgaussian: Vast 3d gaussians for large scene reconstruction. In Proceedings of the IEEE/CVF Conference on Computer Vision and Pattern Recognition (pp. 5166-5175). DOI: 10.1109/CVPR52733.2024.00494
- [22]K. Cheng, X. Long, K. Yang, Y. Yao, W. Yin, Y. Ma, et al., (2024, January). Gaussianpro: 3d gaussian splatting with progressive propagation. In Forty-first International Conference on Machine Learning.
- [23]Z. Zhang, W. Hu, Y. Lao, T. He, and H. Zhao, (2024). Pixel-gs: Density control with pixel-aware gradient for 3d gaussian splatting.
- [24]C. Yan, D. Qu, D. Xu, B. Zhao, Z. Wang, D. Wang, et al., (2024). Gs-slam: Dense visual slam with 3d gaussian splatting. In Proceedings of the IEEE/CVF Conference on Computer Vision and Pattern Recognition (pp. 19595-19604). DOI: 10.1109/CVPR52733.2024.01853
- [25]Mitsuhashi, K., Hashimoto, H., & Ohyama, Y. (2015). Motion Curved Surface Analysis and Composite for Skill Succession using RGBD Camera. Proceedings of the 12th International Conference on Informatics in Control, Automation and Robotics, 406–413. https://doi.org/10.5220/0005569904060413
- [26]Gruber, M., & Walcher, W. (2014). CALIBRATING THE NEW ULTRACAM OSPREY OBLIQUE AERIAL SENSOR. The International Archives of the Photogrammetry, Remote Sensing and Spatial Information Sciences, XL-3/W1, 47–52. https://doi.org/10.5194/isprsarchives-xl-3-w1-47-2014
- [27]Aldyan, F. (2018). KAJIAN TUTUPAN LAHAN BERBASIS OBYEK MENGGUNAKAN DATA UAV TRIMBLE UX5 (WILAYAH STUDI: DESA PAGAK, KAB. PURWOREJO JAWA TENGAH). Seminar Nasional Geomatika, 2, 517. https://doi.org/10.24895/sng.2017.2-0.449
- [28] Wang, J. (2000). An airborne multi-angle TIR/VNIR imaging system. Remote Sensing Reviews, 19(1-4), 161-169. https://doi.org/10.1080/02757250009532416
- [29]Kacenelenbogen, M., Léon, J.-F., Chiapello, I., & Tanré, D. (2006). Characterization of aerosol pollution events in France using ground-based and POLDER-2 satellite data. Atmospheric Chemistry and Physics, 6(12), 4843–4849. https://doi.org/10.5194/acp-6-4843-2006
- [30]Franzini, M., Casella, V. M., & Monti, B. (2023). Assessment of Leica citymapper-2 lidar data within Milan's Digital Twin Project. Remote Sensing, 15(21), 5263. https://doi.org/10.3390/rs15215263
- [31] Yong, P., Tao, Y., Wen, J., Xiaojun, L., Zengyuan, L., Anmin, F., Fayun, W., Xiaotong, L., Xinwei, Z., Jin, H., & Tao, H. (2023). TECIS: The first mission towards forest carbon mapping by combination of lidar and multiangle optical observations. IGARSS 2023 2023 IEEE International Geoscience and Remote Sensing Symposium, 1890–1893. https://doi.org/10.1109/igarss52108.2023.10282849
- [32]C. Bai, R. Fu, and X. Gao, (2024, May). Colmap-pcd: An open-source tool for fine image-to-point cloud registration. In 2024 IEEE International Conference on Robotics and Automation (ICRA) (pp. 1723-1729). IEEE. DOI: 10.1109/ICRA57147.2024.10611582
- [33]J. T. Barron, B. Mildenhall, M. Tancik, P. Hedman, R. Martin-Brualla, and P. P. Srinivasan, (2021). Mip-nerf: A multiscale representation for anti-aliasing neural radiance fields. In Proceedings of the IEEE/CVF international conference on computer vision (pp. 5855-5864). DOI: 10.1109/ICCV48922.2021.00580
- [34]J. T. Barron, B. Mildenhall, D. Verbin, P. P. Srinivasan, and P. Hedman, (2022). Mip-nerf 360: Unbounded anti-aliased neural radiance fields. In Proceedings of the IEEE/CVF conference on computer vision and pattern recognition (pp. 5470-5479).
- [35]R. Martin-Brualla, N. Radwan, M. S. Sajjadi, J. T. Barron, A. Dosovitskiy, and D. Duckworth, (2021). Nerf in the wild: Neural radiance fields for unconstrained photo collections. In Proceedings of the IEEE/CVF conference on computer vision and pattern recognition (pp. 7210-7219).
- [36]M. Tancik, V. Casser, X. Yan, S. Pradhan, B. Mildenhall, P. P. Srinivasan, et al., (2022). Block-nerf: Scalable large scene neural view synthesis. In Proceedings of the IEEE/CVF Conference on Computer Vision and

- Pattern Recognition (pp. 8248-8258). DOI: 10.1109/CVPR52688.2022.00807
- [37]H. Turki, D. Ramanan, and M. Satyanarayanan, (2022). Mega-nerf: Scalable construction of large-scale nerfs for virtual fly-throughs. In Proceedings of the IEEE/CVF Conference on Computer Vision and Pattern Recognition (pp. 12922-12931). DOI: 10.1109/CVPR52688.2022.01258
- [38]Y. Xiangli, L. Xu, X. Pan, N. Zhao, A. Rao, C. Theobalt, et al., (2022, October). Bungeenerf: Progressive neural radiance field for extreme multi-scale scene rendering. In European conference on computer vision (pp. 106-122). Cham: Springer Nature Switzerland.
- [39]R. Marí, G. Facciolo, and T. Ehret, (2022). Sat-nerf: Learning multi-view satellite photogrammetry with transient objects and shadow modeling using rpc cameras. In Proceedings of the IEEE/CVF Conference on Computer Vision and Pattern Recognition (pp. 1311-1321). DOI: 10.1109/CVPRW56347.2022.00137
- [40]Wei, P., Yan, L., Xie, H., Qiu, D., Qiu, C., Wu, H., ... & Huang, M. (2024). LiDeNeRF: Neural radiance field reconstruction with depth prior provided by LiDAR point cloud. ISPRS Journal of Photogrammetry and aerial remote sensing, 208, 296-307.
- [41]K. Deng, A. Liu, J. Y. Zhu, and D. Ramanan, (2022). Depth-supervised nerf: Fewer views and faster training for free. In Proceedings of the IEEE/CVF Conference on Computer Vision and Pattern Recognition (pp. 12882-12891). DOI: 10.1109/CVPR52688.2022.01254
- [42]J. C. Lee, D. Rho, X. Sun, J. H. Ko, and E. Park, (2024). Compact 3d gaussian representation for radiance field. In Proceedings of the IEEE/CVF Conference on Computer Vision and Pattern Recognition (pp. 21719-21728). DOI: 10.1109/CVPR52733.2024.02052
- [43]Fan, Z., Wang, K., Wen, K., Zhu, Z., Xu, D., & Wang, Z. (2023). LightGaussian: Unbounded 3D Gaussian Compression with 15x Reduction and 200+ FPS. ArXiv, abs/2311.17245.
- [44]Ye, Z., Li, W., Liu, S., Qiao, P., & Dou, Y. (2024). AbsGS: Recovering fine details in 3D gaussian splatting. Proceedings of the 32nd ACM International Conference on Multimedia, 1053–1061. https://doi.org/10.1145/3664647.3681361
- [45]Xiaoye Liu. (2008). Airborne LiDAR for DEM generation: Some critical issues. Progress in Physical Geography: Earth and Environment, 32(1), 31–49. https://doi.org/10.1177/0309133308089496
- [46] Vosselman, G., Gorte, B. G., Sithole, G., & Rabbani, T. (2004). Recognising structure in laser scanner point clouds. International archives of photogrammetry, aerial remote sensing and spatial information sciences, 46(8), 33-38.
- [47]Zhou, K., Hou, Q., Wang, R., & Guo, B. (2008). Real-time KD-tree construction on graphics hardware. ACM Transactions on Graphics, 27(5), 1–11. https://doi.org/10.1145/1409060.1409079
- [48]Groves, P. D. (2015). Principles of GNSS, inertial, and multisensor integrated navigation systems, 2nd edition [Book review]. IEEE Aerospace and Electronic Systems Magazine, 30(2), 26–27. https://doi.org/10.1109/maes.2014.14110
- [49]W. Hugemann, (2010). Correcting lens distortions in digital photographs. Ingenieurbüro Morawski+ Hugemann: Leverkusen, Germany, 20.
- [50]J. P. de Villiers, F. W. Leuschner, and R. Geldenhuys, (2010, January). Modeling of radial asymmetry in lens distortion facilitated by modern optimization techniques. In Intelligent Robots and Computer Vision XXVII: Algorithms and Techniques (Vol. 7539, pp. 190-197). SPIE. DOI: 10.1117/12.838804
- [51]M. Bleyer, C. Rhemann, and C. Rother, (2011, August). Patchmatch stereo-stereo matching with slanted support windows. In Bmvc (Vol. 11, pp. 1-11). DOI: 10.5244/C.25.14
- [52]L. Lin, Y. Liu, Y. Hu, X. Yan, K. Xie, and H. Huang, (2022, October). Capturing, reconstructing, and simulating: the urbanscene3d dataset. In European Conference on Computer Vision (pp. 93-109). Cham: Springer Nature Switzerland. DOI: 10.1007/978-3-031-20074-8_6
- [53]C. Wang, J. Sun, L. Liu, C. Wu, Z. Shen, D. Wu, et al., (2023, October). Digging into depth priors for outdoor neural radiance fields. In Proceedings of the 31st ACM International Conference on Multimedia (pp. 1221-1230). DOI: 10.1145/3581783.3612306